Observed Wind and SST Variability off the California Coast During Summertime High Wind Events

Weiguang Wu[1], Ana Beatriz Villas Boas[2], and Sarah T. Gille[3]

[1]Massachusetts Institute of Technology
[2]Scripps Institution of Oceanography
[3]University of California, San Diego

November 23, 2022

Abstract

Sea surface winds off the California coast are characterized by high wind events that occur in spring and summer. In June, a well-defined wind event region is formed off the five major capes, extending ~300km offshore. In the present work, a satellite wind product is used to study the spatial variability of these wind events. High-speed and long-duration events primarily occur off Cape Mendocino, whereas low-speed and short-duration events are more uniformly distributed over the wind event region. Coastal buoy observations show an anti-correlation between wind speed and sea surface temperature (SST) during wind events: a decrease in wind speed accompanies an increase in SST before the start of events, and an increase in wind speed accompanies a decrease in SST after the start of events. Different SST cooling patterns are observed within different categories of wind events: (1) High-speed events lead to more SST cooling compared to low-speed events. (2) Long-duration events lead to longer SST cooling times compared to short-duration events. SST cooling is observed both at nearshore buoy locations and at locations far from the coast. The magnitude of cooling is about 1°C nearshore and 0.3°C offshore. A case study of upper-ocean responses from mooring observations suggests that a combination of enhanced wind-driven mixing and Ekman pumping processes may explain SST cooling nearshore during wind events.

Observed Wind and SST Variability off the California Coast During Summertime High Wind Events

Weiguang Wu[1,2], Ana. B. Villas Bôas[1], and Sarah. T. Gille[1]

[1]Scripps Institution of Oceanography, University of California San Diego, La Jolla, CA, USA
[2]Now at MIT-WHOI Joint Program in Oceanography/Applied Ocean Sciences and Engineering, Massachusetts Institute of Technology, Cambridge, MA, USA

Key Points:

- Wind events exceeding 9 m/s are a characteristic feature off the California coast in spring/summer.
- High wind events lead to sea surface temperature cooling at both nearshore and offshore buoy locations.
- The sea surface temperature response to wind events depends on the event duration and the strength of wind speed.

Corresponding author: Weiguang Wu, `weiguang@mit.edu`

Abstract

Sea surface winds off the California coast are characterized by high wind events that occur in spring and summer. In June, a well-defined wind event region is formed off the five major capes, extending ∼300 km offshore. In the present work, a satellite wind product is used to study the spatial variability of these wind events. High-speed and long-duration events primarily occur off Cape Mendocino, whereas low-speed and short-duration events are more uniformly distributed over the wind event region. Coastal buoy observations show an anti-correlation between wind speed and sea surface temperature (SST) during wind events: a decrease in wind speed accompanies an increase in SST before the start of events, and an increase in wind speed accompanies a decrease in SST after the start of events. Different SST cooling patterns are observed within different categories of wind events: (1) High-speed events lead to more SST cooling compared to low-speed events. (2) Long-duration events lead to longer SST cooling times compared to short-duration events. SST cooling is observed both at nearshore buoy locations and at locations far from the coast. The magnitude of cooling is about 1°C nearshore and 0.3°C offshore. A case study of upper-ocean responses from mooring observations suggests that a combination of enhanced wind-driven mixing and Ekman pumping processes may explain SST cooling nearshore during wind events.

Plain Language Summary

Strong sea surface winds are a common phenomenon along the coast of California in summertime. The predominant northerly winds are intermittently interrupted by periods of weakening of wind speed caused by passing storms. These fluctuations lead to a series of high wind events occurring off the five major capes in spring and summer. In this study, we use a satellite wind product and coastal buoy observations to study these wind events. Wind events can be characterized based on their duration and the wind speed magnitude during the event. We find that both high-speed and long-duration events occur primarily off Cape Mendocino, whereas low-speed and short-duration events are more uniformly distributed over the wind event region. Buoy observations show that a decrease in wind speed corresponds to an increase in sea surface temperature (SST), while an increase in wind speed corresponds to a decrease in SST. SST cooling is observed both close to the coast and offshore, indicating that the cooling mechanism is not specific to the coastal regions. Based on a case study from ocean mooring observations, we hypothe-

size that a combination of enhanced wind-driven mixing and coastal upwelling processes are likely to explain SST cooling nearshore during wind events.

1 Introduction

Summertime winds off the California coast are primarily driven by a pressure gradient between the North Pacific High (NPH) and a thermal low over the southwest United States (Halliwell & Allen, 1987). This pressure gradient results in predominantly alongshore, upwelling-favorable winds that tend to cool the sea surface, reducing the thickness of the marine atmospheric boundary layer (MABL) (Koračin & Dorman, 2001; Dorman et al., 2000, 2013). The alongshore flow in the MABL interacts with a series of capes along the California coast (see Figure 1), causing the wind to decelerate on the upwind side of the capes and accelerate on the downwind side, giving rise to a phenomenon known as "expansion fan" winds (Edwards et al., 2001; Koračin et al., 2004).

The predominant northerly winds that are typical in spring and summer are intermittently interrupted by periods of weakening or even reversal caused by synoptic atmospheric systems. These fluctuations in the characteristic winds produce a cycle of alternating expansion fan winds and relaxation events. Fewings et al. (2016) proposed that these event cycles span about 12 days and that they happen in three stages: (1) Synoptic propagating cyclones weaken the predominant upwelling-favorable winds off Oregon/northern California. (2) After the cyclones propagate beyond the northward portion of the NPH, the NPH extends to the northeast, and the northerly wind intensifies along the coast of central California. (3) The northeast extension of the NPH advects warm desert air offshore, winds relax off the southern California coast, and the wind relaxation extends to northern California.

The question of how wind events impact SST variability in the California Current System (CCS) has been investigated in previous studies. The summer mean SST in the CCS is mainly the result of wind-driven coastal upwelling. Along the coast, positive wind-stress curl induces Ekman pumping, upwelling cold water toward the surface. This Ekman pumping increases during wind intensification and reduces during the wind relaxation stage (e.g. Taylor et al., 2008; Flynn et al., 2017). Besides the Ekman pumping mechanism, the net surface heat flux affected by the winds also contributes to SST variability in the three-stage wind cycle (Flynn et al., 2017). During stage 1 (wind relaxations), SST warming off the coast of Oregon/northern California is caused mostly by reduced latent cooling due to weakened winds and by increased shortwave radiation due to decreased cloudiness. However, the net heat flux is not the main driver of SST variability near the coast during stage 2 (wind intensification) and stage 3 (southern wind relaxations), when changes in the rates of wind-driven mixing and Ekman pumping may play major roles. Another possible mechanism that changes SST is horizontal advection. The weakening or intensification of equatorward winds during wind events can lead to increased warm poleward flow or cold equatorward flow in the ocean along the California coast (e.g. Send et al., 1987; Chelton et al., 1988; Melton et al., 2009). Moreover, nonlinear effects become more important at smaller scales. The change of wind patterns over a relatively short period of time may influence the rate of nonlinear Ekman pumping through eddy-wind interactions (McGillicuddy et al., 2007) and may modify submesoscale SST frontal structures (Thomas & Lee, 2005).

Although some recent satellite-based studies have explored the evolution of wind events and the corresponding upper-ocean response (e.g. Taylor et al., 2008; Melton et al., 2009; Fewings et al., 2016; Flynn et al., 2017), the spatial variability of these events and a more detailed characterization of their climatology remain unclear. Buoy-based wind and SST measurements provide a consistent and long-enough temporal record that allows us to further separate the wind events into different categories (e.g. long vs short, strong vs weak) and to explore nuances of the SST response to these events. In the present study, we first identify wind events based on wind speed and wind direction (section 2.4). We then assess the spatial and seasonal evolution of these events in the CCS (section 3.1), and characterize the statistics of different categories of wind events (section 3.2). In section 3.3, we use buoy measurements to study SST variability within wind events, and we explore the relationship between SST and the duration and strength of wind events (section 3.4). Finally, in section 4, we explore possible mechanisms that could explain wind/SST variability during these wind events.

2 Data and Methods

2.1 CCMP Surface Ocean Vector Winds

The Cross-Calibrated Multi-Platform (CCMP v2.0) gridded surface vector wind dataset (Atlas et al., 2011; Mears et al., 2019) is an analysis product produced by Remote Sensing Systems (RSS). CCMP v2.0 uses a variational analysis method to combine version-7 of RSS radiometer wind speeds, QuikSCAT and ASCAT scatterometer wind vectors, moored buoy wind measurements, and ERA-Interim model wind fields. The final global product provides 6-hourly gap-free 10 m ocean vector winds, with a spatial resolution of 0.25°×0.25° in latitude and longitude. It is available from 1987 to the present. In this study, we use CCMP v2.0 6-hourly winds from 2002 to 2015 off the California coast, in the region extending over 25°–45°N and 110°–140°W.

2.2 NDBC Buoy Measurements

To study the effects of high wind events on SST variability, we use meteorological buoy measurements from the National Data Buoy Center (NDBC), which reports hourly 4-m wind speed with an accuracy of ±1 m s^{-1} and wind direction with an accuracy of ±10°. NDBC wind speeds are converted from 4 m to 10 m using a power law scaling (Hsu et al., 1994). The NDBC buoys also provide hourly measurements of SST. Buoy temperature sensors are located about 0.7 m below the water line and have an accuracy of ±1°C. For this study, six NDBC buoys in the CCS region are selected with record lengths ranging from 18 to 32 years. The locations of these buoys are shown in Figure 1. Table 1 lists the geographic coordinates, time span, and distance to coast for each buoy. Since diurnal variability is not the focus of this study, and the wind events that we study occur over time scales of days and weeks, a low-pass Hanning filter with cutoff frequency of $(36\ \mathrm{hr})^{-1}$ is applied to the 10-m wind speed and sea surface temperature time series. We select data from April to July when wind events are prevalent (Figure 3). The low-pass filtered data for each four-month spring segment are also detrended to remove the seasonal trend.

2.3 CCE Mooring Measurements

A case study discussed in section 4 uses upper-ocean measurements from CCE-2 (e.g. Ohman et al., 2013; Martz et al., 2014), one of moorings of the California Current Ecosystem (CCE) project. The mooring is located about 30 km southwest of Point Conception, where the water depth is about 800 m (Figure 3). MicroCAT sensors on CCE2 measure water temperature and salinity every half hour at depths of 7 m, 15 m, 26 m, 46 m. Here we use measurements at these depths from the 3rd and 4th deployments of CCE2 (CCE2-03/04) from March 2012 to May 2014. For each depth, we calculate the potential temperature and density (referenced to 2000 m) using the TEOS-10 seawater toolbox (McDougall & Barker, 2011). For consistency, the data are low-pass filtered with a cutoff timescale of 36 hr.

2.4 Definition of High Wind Events

Previous studies have defined wind events in different ways. For example, Melton et al. (2009) identified the onset of southern wind relaxations by finding the zero crossings of the time amplitude for the first empirical orthogonal function of the 36 hr low-pass filtered along-principal-axis wind speed at four NDBC buoys near Pt. Conception, and they required the speed to exceed the mean at least 70% of the time for 3 days before the onset and to be below the mean at least 60% of the time for 2.5 days after the onset. Fewings et al. (2016) and Flynn et al. (2017) adopted the definition from Melton et al. (2009) to study the 12-day evolution of the three-stage wind events and the SST response to these wind events. In contrast, Taylor et al. (2008) used NDBC buoy winds to define wind intensification events as occurring when the along-principal-axis wind speed exceeds the 75th percentile of the monthly wind distribution for at least 18 hrs over a 35-hr period.

In this study, we relax these previous definitions to find high-speed wind events from April to July according to the following method: we fix the wind speed threshold to be 9 m s^{-1}, which is the 90th percentile of CCMP wind speeds in June from 2002 to 2015 within the study region (25°–45°N and 110°–140°W). This wind speed threshold is used for every grid point in the domain for any given month. Here we define a wind event as the time period when the wind speed exceeds the 9 m s^{-1} threshold with wind direction coming from 270° to 360° (with 360° representing northerly winds) for at least 36 hrs (6 consecutive CCMP data points). The start of a wind event occurs when the wind speed first exceeds the 9 m s^{-1} threshold. One such event occurred in May 2005 at 35.625° N, 121.875° W (Figure 2a). The blue area of Figure 2a indicates the evolution of the event.

We apply the same wind event definition to the four near-shore NDBC buoys, 46014, 46013, 46026, and 46028, except that we allow hourly wind speed to drop below 9 m s^{-1} threshold occasionally (less than 6 hrs) during the event. In Figure 2b, we show the NDBC buoy 46028 representation of the event in Figure 2a, with CCMP and buoy locations chosen to be as close as possible to each other spatially. The red area indicates the evolution of the event. CCMP suggests a slightly later start time than the buoy, which we attribute to the coarse temporal resolution of the CCMP wind product. Wind events observed by the buoys also show an overall higher wind speed than CCMP wind events. For the offshore buoys (46006 and 46059), where the summer wind speed is relatively weak (Figure 1), wind events are not a dominant phenomena during the spring and summer, yet wind events with relatively high wind speed can still be observed. These events are likely associated with propagating storms. Since the wind direction is highly variable during high wind speed events at these off-shore locations, we impose no restriction on the wind direction but keep the 9 m s^{-1} wind speed threshold to identify the offshore high-wind events.

2.5 Composite Wind Speed/SST

To capture the mean evolution of wind events at a single buoy location, we construct composite means of wind speed and SST for every hour from 96 hrs before the onset of the event (negative lag) to 96 hrs after the onset (positive lag), making in total a 193-hr time period, regardless of the duration of each individual event. To do this, we average wind speed/SST at every lag hr over all wind events to obtain the composite mean of wind speed (blue lines, Figure 5,6) and SST (red lines, Figure 5,6). Events with missing data are not included in the analysis. There are 225 valid wind events for buoy 46014, 280 events for 46013, 141 events for 46012, 265 events for 46028, 158 events for 46006, 113 events for 46059. Uncertainties (shaded areas in Figures 5 and 6) correspond to one standard error of the mean of wind speed/SST at each lag hr.

3 Results

3.1 Spatial and Seasonal Variability of Wind Events

For every CCMP grid point in the region (28°–43°N, 110°–135°W), we find all wind events from 2002 to 2015 using the definition described in section 2.4. Then, we calculate the monthly cumulative duration by summing the duration of individual events that occurred in each month, and plot the average monthly cumulative duration of wind events between 2002 and 2015 (Figure 3). Thus, the "cumulative duration" at each location represents the average number of days within a month when there are wind events. To show the seasonal variability of wind events, we also show the maps in fall and winter when wind events are less common. Based on the June map when wind events are most common, we define the "wind event region" to be where the average monthly cumulative duration exceeds 7 days (red contour line).

High winds off the California coast vary both spatially and seasonally, as shown in Figure 3. From November to January, the averaged cumulative duration per month ("cumulative duration", hereinafter) is small: most of the wind events occur off Point Conception, with a cumulative duration less than 5 days. From February to March, wind events start to grow in the lees of Cape Mendocino and Point Conception with a cumulative duration of about 8 days, and an embryonic structure of expansion fan winds can be seen at these two major capes. The structure continues to grow and becomes well-developed in June from the California-Oregon border to southern California, extending roughly 300 km offshore. A clear expansion fan wind signature is revealed at the five major capes (from north to south): Cape Blanco, Cape Mendocino, Point Arena, Point Sur, and Point Conception. The average cumulative duration within the wind event region is about 7 days in April, 9 days in May, and 11 days in June. The maximum occurs off Cape Mendocino in June with a cumulative duration of about 17 days. After June, the cumulative duration of wind events decreases off Point Sur and Point Conception. The average cumulative duration per month within the wind event region drops to about 7 days, while wind events off Cape Mendocino remain relatively common with cumulative duration exceeding 10 days. The cumulative duration gradually decays in fall; the average cumulative duration within the region in September is about 4 days. From September to November, the region of high cumulative duration off Cape Mendocino starts to disappear, while events off Point Conception start to become more common with cumulative duration between 3 and 5 days.

3.2 Classifying Wind Events: Speed and Duration

Although wind events are defined to have speeds greater than 9 m s^{-1} for at least 36 hrs, the duration and wind speed maximum of each event vary substantially, with the longest event lasting over two weeks and the most extreme event having a maximum wind speed of $\sim$30 m s^{-1}. To better understand speed–duration statistics, we sort April–July, 2002-2015 CCMP wind events into three categories based on the event duration and the magnitude of wind speed:

- **Low-speed vs high-speed.** Events are classified as "low-speed" if the 90th percentile of wind speeds during the event is less than 15 m s^{-1}, while for "high-speed" events the 90th percentile of wind speeds exceeds 15 m s^{-1};
- **Short-duration vs long-duration.** Events are classified as "short-duration" if the duration of the event is less than 72 hrs, while "long-duration" events last more than 72 hrs;
- **Low-speed long-duration vs high-speed short-duration.** Events are classified as "low-speed long-duration" if the duration is greater than 72 hrs and the 90th percentile of wind speeds is less than 15 m s^{-1}, while "high-speed short-duration" events last less than 72 hrs but have the 90th percentile of wind speeds greater than 15 m s^{-1}.

Table 2 summarizes the statistics of the three categories of wind events. Within the wind event region (outlined by the red contour, Figure 3), 64% of events have a duration less than 72 hrs, and 36% have a duration greater than 72 hrs. While short-duration events (< 72 hrs) occur more frequently than long-duration events (>72 hrs) from April to July, long-duration events contribute more to the total wind-event time in the wind event region: short-duration events account for 43% of total wind-event time, and long-duration events account for 57%. The percentage of total wind-event time is the sum of the duration time of the events of a given category, computed for CCMP grid points within the wind-event region, divided by the sum of duration time of all events defined in section 2.4 within the wind-event region. Despite differences in the definition of wind events, our results are consistent with those of Taylor et al. (2008), who also found, using a point buoy measurement (NDBC 46014), that long-duration events are less frequently occurring but contribute more to the wind-event time.

For events with different wind-speed magnitudes, 90% of total wind-event time and 93% of the events correspond to low-speed events, with 90th percentile wind speeds less than 15 m s^{-1}. Low-speed long-duration events comprise 32% of number of events and 49% of total wind-event time. In contrast, high-speed short-duration events account for only 3% of events and 2% of total wind-event time. Following the same steps discussed in section 3.1, in Figure 4 we show the spatial variability of cumulative duration of these three wind-event categories. The maps are averaged from April to July between 2002 and 2015. Both low-speed and short-duration events (Figure 4a,b) are well distributed along the wind event region, extending ∼300 km off shore, whereas most high-speed and long-duration events (Figure 4d,e) occur off Cape Mendocino. Compared to low-speed events (Figure 4a), high-speed events (Figure 4d) are confined closer to the coast, and compared to other events categories, high-speed short-duration events (Figure 4f) have much less cumulative duration and occur mostly at Cape Blanco, Cape Mendocino, and Pt Arena.

3.3 Evolution of Composite Wind Speed and Sea Surface Temperature

To understand the evolution of wind speed and the SST response during the wind events, we focus on four nearshore NDBC buoys within the wind event region. The composite mean of wind speed (blue lines, Figure 5) shows that wind events follow a distinct evolution pattern. At negative lags, the composite wind speeds are below the 9 m s^{-1} threshold, with an average minimum speed of 6–7 m s^{-1} occurring 17 to 20 hrs prior to the identified onset of the wind event. As the wind event starts (lag 0 hr), the wind speed increases rapidly and peaks between 24 and 28 hrs after wind onset, with the averaged maximum speed of 12–13.5 m s^{-1} depending on the buoy location. In a period less than 48 hrs, the composite wind speed increases ∼6 m s^{-1}. This pattern of anomalously low wind speed before the wind event and peak wind speeds occurring ∼24 hrs after the start of the event is consistent with results of Taylor et al. (2008). After the peak, the wind speed gradually falls toward the 9 m s^{-1} threshold. This cycle of weakening, intensifying, and then weakening for winds during the 193-hr event composite is also consistent with results from Fewings et al. (2016), who revealed, from QuickSCAT observations, a similar three-stage cycle of wind events spanning about 12 days along the California coast in summertime.

The composite mean of SST (red lines, Figure 5) evolves in opposition to wind speed: at negative lags, composite SST gradually increases as wind speed decreases and peaks between lag -9 hr and -12 hr with maximum SST 10.5-12°C. Compared to SST at lag -96 hr, a 0.3-0.5°C warming can be observed at four buoy locations. The maximum of SST lags the minimum of wind speed by about 8 hrs. As the wind speed steadily increases, SST decreases continuously until about lag +48 hr, about 24 hrs after the peak of wind speed. Among the four buoys, the largest 1.2°C cooling of SST (with respect to SST maximum) occurs at buoy 46014, and the least cooling is 0.75°C at buoy 46012. After lag +48 hr, SST remains anomalously cold, except at buoy 46014 where a slight warming trend is observed. A similar pattern of decreasing SST with increasing wind speed is also observed at two far offshore sites, buoy 46006 and 46059 (red lines, Figure 6) but with a smaller range of cooling (about 0.3°C at buoy 46006 and 0.4°C at buoy 46059) compared to cooling observed at the four nearshore buoys. At all six buoy sites, a decrease in wind speed typically corresponds to an increase in SST before the wind events start, and an increase in wind speed corresponds to a decrease in SST after the start of event.

3.4 SST Response to Categories of Wind Events

Overall, the temporal evolution of composite wind speed and SST is consistent across the four coastal buoys during the wind events. However, the relationship between wind speed and SST can be sensitive to wind-event duration and the magnitude of the wind speed. To investigate this relationship, based on the definition described in section 3.2, we classify NDBC wind events into three categories: (1) low-speed vs high-speed; (2) short-duration vs long-duration; (3) low-speed long-duration vs high-speed short-duration. For each scenario, the resulting composite mean wind speed (green dashed lines) and SST (orange dashed lines) at buoy 46014 are shown in Figure 7. These are compared with the average over all events for wind speed (blue solid lines) and SST (red solid lines).

Before the onset of a wind event, wind speed and SST (dashed lines) show consistent patterns in all cases: wind speed decreases, while SST increases. The maximum SST (∼11°C) and the minimum wind speed (∼7 m s^{-1}) are similar to those obtained from averaging all events (solid lines). After the onset of an event, the evolution varies depending on the category of event.

Wind speed anomalies appear anti-correlated with SST anomalies. For low-speed events (Figure 7a), the composite mean of wind speed (green dashed line) is lower than the mean from averaging all events (blue solid line), while the composite mean of SST (orange dashed line) is warmer than the all-event average (red solid line). For high-speed events (Figure 7d), the wind speed is greater than the all-event average, while SST is colder than the all-event average. Similar patterns emerge at the other three nearshore buoys locations (panels a and d in Figures S1–S3): lower wind speeds consistently correspond to higher SSTs and vice versa. This relationship is also identifiable when comparing short-duration events to high-speed short-duration events (panels b and f in Figures 7, S1–S3). The wind speed at all buoy locations peaks at about lag +24 hr, and SST has a minimum between lag +36-48 hr, implying a 12-24 hr offset between the wind and SST extrema. A higher wind speed maximum for high-speed short-duration events leads to a lower SST minimum compared to the SST minimum for all short-duration events. However, uncertainties are large compared with differences, and more wind events might be needed to obtain a more robust result.

The duration of wind events also impacts the SST response. Both short-duration and long-duration events (Figure 7b,e) at buoy 46014 show wind-speed evolution consistent with the all-event average (blue solid line) until 24 hrs after the event starts. After lag +24 hr, the wind speed for short-duration events weakens quickly, whereas the wind speed for long-duration events sustains high speeds through the end of the composite. The SST response (Figure 7e) reveals that at positive lags, long-duration events lead to continuously SST cooling of about 1.5°C with respect to the SST maximum. The pattern of longer wind duration responding to longer cooling time can also be seen at the other three nearshore buoy locations (Figures S1e, S2e, S3e). At buoy 46014 (Figure 7b), the weakening of wind speed after lag +24 hr corresponds to the warming of SST after lag +48 hr. At the other three buoy locations, SST warming occurs around lag +36 hr (Figures S1b, S2b, S3b). At the end of the composite, SST is finally restored roughly to the initial value. A similar relationship between the duration of high wind speed and the duration of SST cooling is also observed in panels c and f.

4 Discussion: What Causes the Change in SST During Wind Events?

Based on the three-stage wind events proposed by Fewings et al. (2016), we expect the evolution of wind speed (blue lines, Figure 5) to be associated with a similar mechanism of wind expansions interrupted by summertime synoptic atmospheric forcing. At the buoy sites, the anti-correlation between SST and wind speed during wind events (Figure 5) is consistent with the satellite-derived results of Flynn et al. (2017), who showed that along the California coast positive SST anomalies follow wind relaxations, and negative SST anomalies follow wind intensification. It remains an open question whether this SST variability is controlled by air-sea heat flux, Ekman transport, wind-induced turbulent mixing, or horizontal advection of SST by ocean currents. Building on some results from Flynn et al. (2017), we will use mooring observations to analyze a case study of upper-ocean response to wind events and explore the mechanisms that could account for the warming and cooling trend of SST.

During the warming phases, our composites show that the SST warms at negative lags before the onset of the events (Figure 5) and in the case of short-duration events, it warms again at positive lags toward the end of the wind event (Figure 7b,f). Flynn et al. (2017) showed that changes in surface heat flux offshore are the main driver of SST warming during wind relaxation events north of 37°N. As the wind speed decreases, the latent cooling is reduced, and due to decreased cloudiness, shortwave radiation increases and longwave radiation is reduced. However, surface heat fluxes offshore do not explain SST warming in response to wind relaxation south of 37°N, where the reduction in shortwave radiation, by increased cloudiness, offsets the reduced latent cooling. As suggested by Flynn et al. (2017), changes in the rate of wind-driven mixing and horizontal advection may play more important roles in explaining the warming there. Additionally, the rate of cold water upwelled as a result of Ekman transport is expected to reduce as the alongshore wind speed decreases. For four of the nearshore buoys in this study, we expect that the reduced upwelling rate also contributes to the observed SST warming pattern.

Similarly to the periods of SST warming, the changes in the rate of coastal upwelling and wind-driven mixing can be important in driving SST cooling. As wind speed increases, enhanced vertical shear strengthens the homogenization between warm sea surface and cold water below, and enhanced wind-stress curl increases the rate of upwelling cold water below. Both mechanisms can lead to surface cooling but would have different signatures within the water column. To explore these two mechanisms, we look at the temporal evolution of upper-ocean water temperature and density during two wind events at the CCE-2 mooring (Figure 8). Both wind events lasted about 50 hrs, and the potential temperature contour plots for both indicate that the near-surface temperature cools after the wind event starts. Reanalysis fields from ERA-Interim at the mooring location indicate that surface heat flux is not the main driver of SST cooling (not shown). The potential temperature over depths evolves differently for the two events: In Figure 8a, the temperature at depth 7-26m cools as the event starts and warms around lag +100 hr, whereas the temperature at depth 26-46m warms as the wind speed increases and cools after lag +100 hr; In Figure 8b, the temperature over all depths cools continuously. Similar to potential temperature, time series of potential density over a range of depths suggest two distinct processes that could explain the cooling. In case a, the convergence of potential density time series from different depths after the wind event starts (i.e. starting around lag +20 hr) is consistent with wind-driven vertical mixing. As wind weakens, the upper 50 m restratifies, and the potential density time series separate (after ∼100 hours). In case b, the potential densities at 7m, 15m, and 26m merge quickly after the wind event starts, indicating mixing, but the water does not homogenize to 46 m depth. Instead the 7-26 m potential density evolves in parallel with the 46 m potential density. The shoaling of potential density time series at all depths in the upper 50 m is consistent with upwelling being the dominant process responsible for SST cooling. Indeed, Taylor et al. (2008) suggest that the upwelling peaks about 48 hours after the start of the wind events, which may also explain the sustained SST cooling after +48 hr lags during the long-duration events (red lines, Figure 7c,e).

Another indicator of enchanced coastal upwelling during wind events comes from the comparison of SST cooling at nearshore and far-offshore buoys. At the farthest offshore buoy 46006, 0.3°C cooling of SST (the difference between minimum and maximum SST) can be observed during wind events (red line, Figure 6a). Among the four nearshore buoys, low-speed events at buoy 46028 show the least SST cooling (0.6°C, red line, Figure S3a). The composite wind speed time series at buoy 46028 (blue line, Figure S3a) has statistics similar to those at buoy 46006 (blue line, Figure 6a) with a mean of ∼10 m s^{-1} and a maximum of ∼12 m s^{-1}. At these two locations, potential temperature and density profiles from an Argo float climatology (Roemmich & Gilson, 2009) also show a similar stratification near the sea surface (Figure S4). This similarity in wind statistics and sea surface stratification suggests that wind-driven mixing at the two locations would induce a similar magnitude of SST cooling. The greater SST cooling observed at buoy 46028, compared to buoy 46006, suggests that other processes, besides wind-driven mixing, also contribute to SST cooling nearshore. Thus, based on the observations from the CCE-2 mooring and 46028 and 46006 buoys, we hypothesize that SST cooling during wind events in nearshore locations result from a combination of enhanced wind-driven mixing and coastal upwelling. Additional processes could also contribute to temperature changes as the wind speed increases. This could include increased equatorward flow of cold water or reduced poleward flow of warm water along the California coast. An array of moorings with current and temperature measurements would be needed to quantify the role of horizontal advection in explaining SST variability during the wind events.

The mechanisms described above focus on the impact of wind on SST. SST can also affect wind. A number of studies have explored mechanisms by which wind accelerates over warmer SST and slows over cooler SST as a result of changes of surface stability, hydrostatic pressure gradients, and momentum transfer (e.g. Samelson et al., 2006; Small et al., 2008). This suggests that warm SST anomalies before the start of the wind event could contribute to subsequent wind speed increases. SST cold anomalies at positive lags may also play a role in explaining the decrease in wind speed about 24 hrs after the onset of wind events (Figure 5). A fully coupled ocean-atmosphere model for the CCS would be needed to quantify the role of air-sea interaction during the wind events.

5 Conclusion

This study has explored spatial and seasonal variability of high wind events along the California coast. Using gridded CCMP wind products, we have shown that most of wind events in winter occur off Point Conception, with a cumulative duration of less than 5 days per month, and then grow off Cape Mendocino in early spring with a cumulative duration of about 8 days per month. A well-developed wind event region is formed in June off the five major capes along the west coast, extending ∼300 km offshore. The average cumulative duration in the region is 11 days per month, and the maximum is about 17 days per month, occurring off Cape Mendocino. Within the wind event region, 7% of wind events are high-speed, with the 90th percentile of wind speeds greater than 15 m s^{-1}. Events lasting longer than 72 hours, classified as long-duration, account for 36% of events. Both high-speed and long-duration events are likely to occur off Cape Mendocino, whereas low-speed and short-duration events are more uniformly distributed over the wind event region. After July, the cumulative duration of wind events decreases to less than 7 days per month south of Point Conception. In northern California, off Cape Mendocino, wind events remain relatively common with monthly cumulative duration exceeding 10 days, and they start to disappear in fall. In winter, the wind events off Point Conception start to become more common with cumulative duration between 3 and 5 days per month.

Composite time series of wind events have been constructed based on NDBC buoy measurements. These composites show that decreases in wind speed accompany increases in SST and vice versa. This pattern is consistent across all six buoys analyzed here. We define wind events as starting when the speed first exceeds 9 m s^{-1}. Under this definition, SST peaks about 10 hrs before the start of the event, and wind speed peaks 24 hrs after the start. During wind events, SST cools by 0.93±0.07°C (from maximum to minimum temperature) averaged over the four nearshore buoys, and 0.33±0.10°C for two far-offshore buoys.

SST cooling patterns are characterized based on the magnitude of the wind speed and the event duration. Strong wind events and long duration wind events can both lead to significant cooling nearshore. Compared to low-speed events, high-speed events lead to more SST cooling. Compared to short-duration events, long-duration events lead to longer SST cooling time. From the SST cooling comparison between nearshore and far-offshore buoy locations, and two cases of upper-ocean responses to wind events at the CCE-2 mooring, we hypothesize that a combination of enhanced wind-driven mixing and Ekman pumping processes are likely to explain SST cooling nearshore during wind events.

Our results have shed light on how the upper-ocean responds to high winds both nearshore and offshore. Although the mooring observations that we analyzed here provided some suggestions of mechanisms contributing to SST cooling, an array of upper-ocean and MBL measurements together with a fully coupled ocean-atmosphere model for the CCS would be necessary to distinguish the roles of surface heat flux, wind-driven mixing, horizontal advection, and Ekman pumping in explaining SST responses to wind events.

Acknowledgments

CCE-2 mooring data were collected by U. Send et al. at the Scripps Institution of Oceanography, funded by the US National Oceanic and Atmospheric Administration, and are accessible through the international OceanSITES program. The Argo float climatology data were collected and made freely available by the International Argo Program and the national programs that contribute to it. The Argo Program is part of the Global Ocean Observing System. This project was supported by NASA grants NNX16AH67G, 80NSSC19K0059, and 80NSSC20K1136. WW was partially funded by N000014-17-1-2390. ABVB was partially funded by NASA Earth and Space Science Fellowship award number 80NSSC17K0326.

Data Availability Statement

CCMP Version-2.0 vector wind analyses are produced by Remote Sensing Systems. Data are available at `http://www.remss.com/measurements/ccmp/`. CCE-2 03/04 data can be accessed at `https://dods.ndbc.noaa.gov/thredds/catalog/data/oceansites/`

Table 1. Station ID, position, depth, time span, and distance to the nearest coast for the selected NDBC buoys along the California coast as well as CCE-2 moorings.

Station ID	Latitude (°N)	Longitude (°W)	Time Span	Distance to Coast (km)
NDBC 46006	40.8	137.48	1983–2013	1090
NDBC 46059	37.98	130.0	1994–2012	540
NDBC 46014	39.22	123.97	1983–2014	20
NDBC 46013	38.23	123.32	1983–2014	20
NDBC 46012	37.36	122.88	1983–2014	20
NDBC 46028	35.74	121.89	1983–2014	40
CCE-2	34.32	120.82	2012–2014	30

DATA/CCE2/catalog.html, and NDBC buoy data are available at https://dods.ndbc.noaa.gov/thredds/catalog/data/stdmet/catalog.html. The Argo float climatology data can be accessed at http://sio-argo.ucsd.edu/RG_Climatology.html.

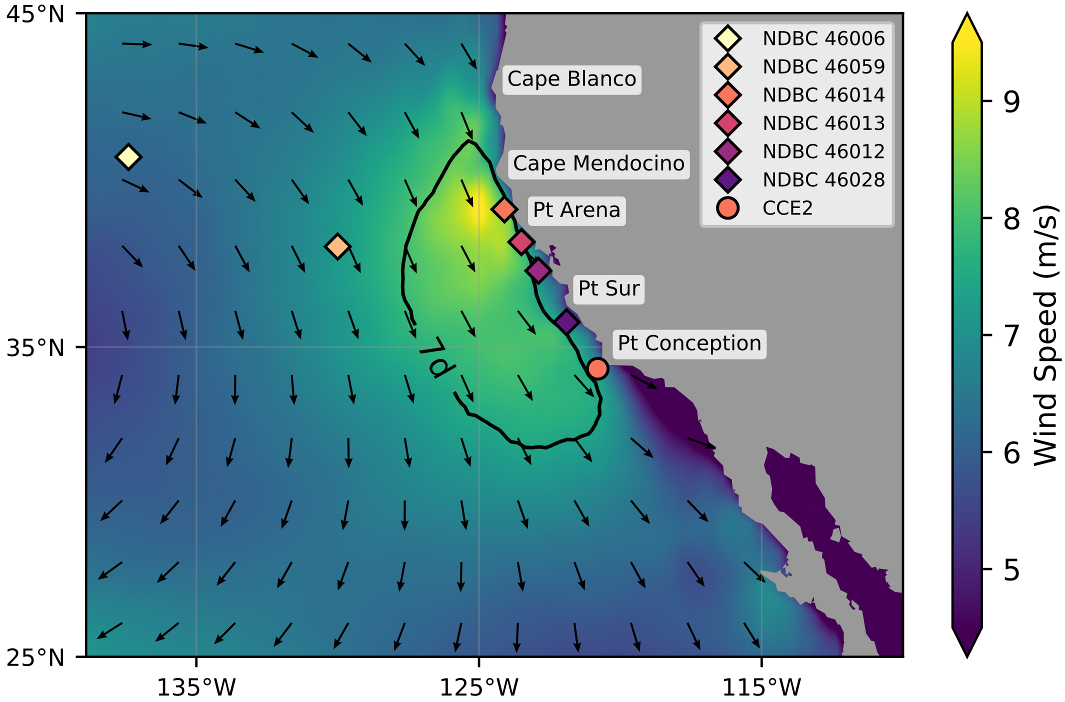

Figure 1. Average wind speed in June from CCMP reanalysis between 2002 to 2015. Colors indicate wind speed, and wind direction is shown as normalized vectors. The locations of six NDBC buoys and CCE-2 mooring, used in this study, are marked. The black contour line outlines the wind event region, which is defined in section 2.4.

Table 2. The percentage of number of events and the total wind-event time for different categories of wind events in the wind event region. The wind event region is outlined by the red contour in Figure 3. The percentage of number of events is the total number of the events of a given category divided by the total number of all events defined in section 2.4, computed for grid points within the wind event region. The percentage of total wind-event time is the sum time of the events of a given category divided by the sum time of all events within the wind event region. The definition for each type of wind events is in section 3.2.

Types of Wind Events	Percentage of Number of Events	Percentage of Total Event Time
Short-duration	64%	43%
Long-duration	36%	57%
Low-speed	93%	90%
High-speed	7%	10%
High-speed short-duration	3%	2%
Low-speed long-duration	32%	49%

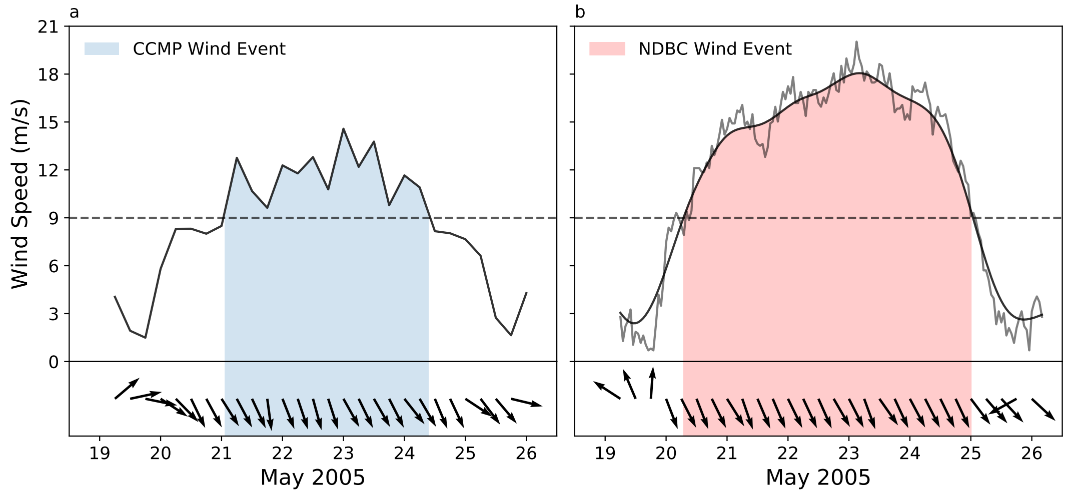

Figure 2. Example time series for a high wind event in May 2005 observed in two different datasets. (a) Time series of CCMP 6-hourly wind speed, along with corresponding wind direction (black arrows), at grid 35.625° N, 121.875° W. (b) Time series of NDBC hourly wind speed, along with the corresponding wind direction (black arrows) plotted at 6-hour spacing, of the same wind event identified at buoy, NDBC 46028 (35.7° N, 121.86° W), in May 2005. The gray line is the raw NDBC wind speed series. The black line is the filtered wind speed. The horizontal dashed line is the 9 m s^{-1} wind speed threshold. The shaded area represents the wind event.

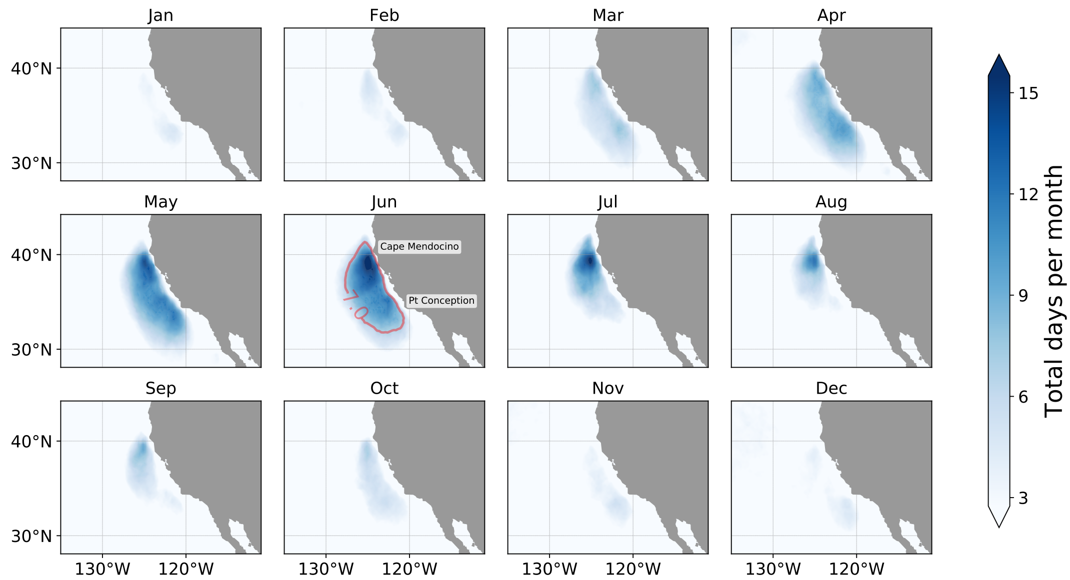

Figure 3. Maps of the average monthly cumulative duration of wind event from CCMP reanalysis between 2002 and 2015. The average cumulative duration (in units of total days per month) indicates the average number of days within a month when wind events occur. The contour of 7 days (red line) in the map of June outlines the wind event region.

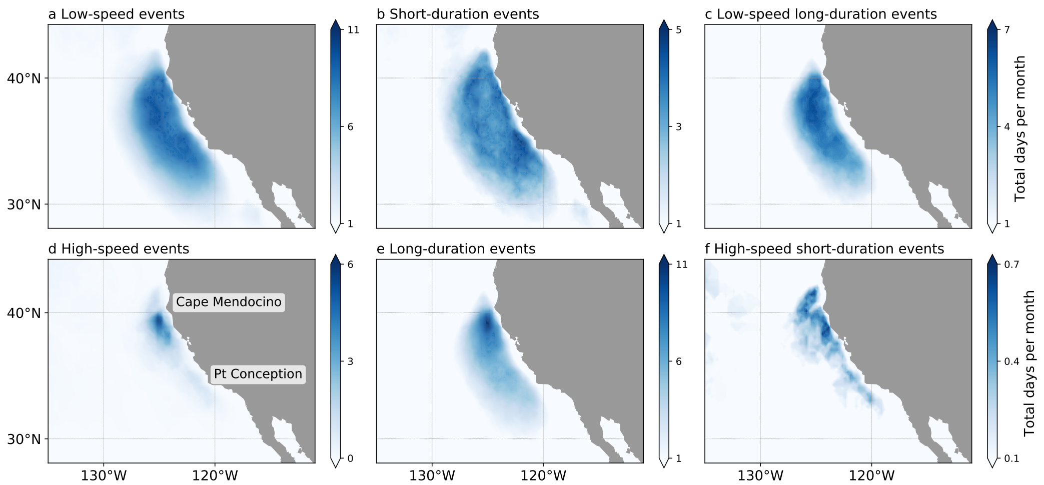

Figure 4. Maps of April-July average cumulative duration for (a) low-speed events, (b) short-duration events, (c) low-speed long-duration events, (d) high-speed events, (e) long-duration events, and (f) high-speed short-duration events. The classification of wind events is discussed in section 3.2. These events are identified from April to July between 2002 and 2015 based on CCMP wind vector reanalysis dataset. The average cumulative duration (in units of total days per month) indicates the average number of days within a month when wind events occur.

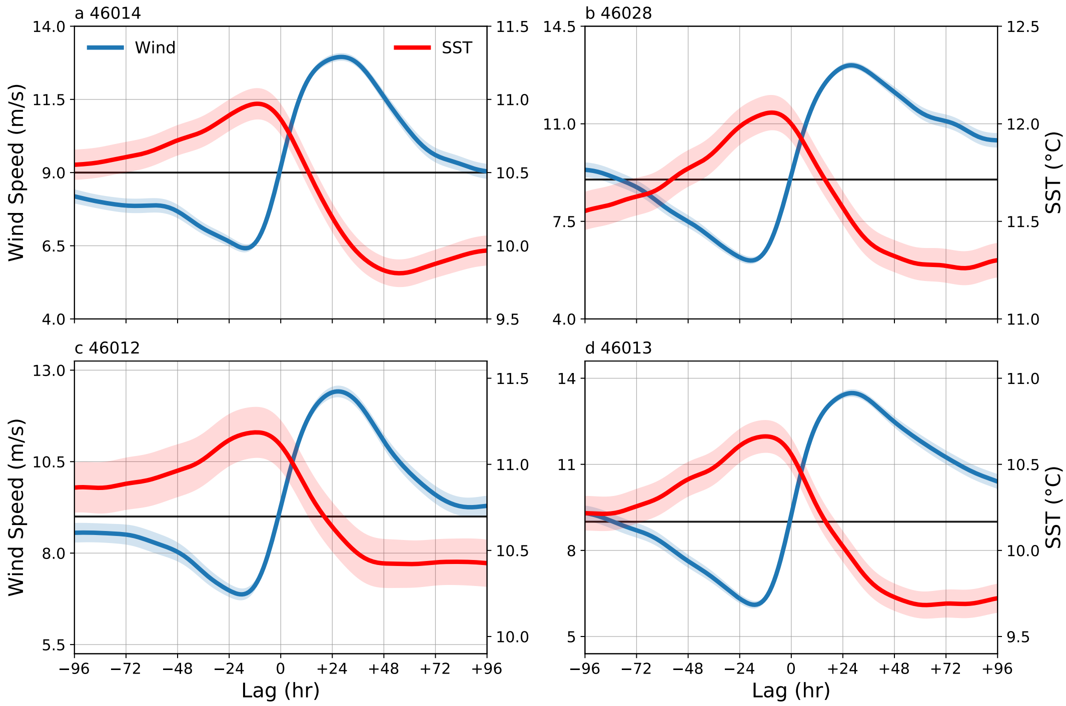

Figure 5. Evolution of composite mean of wind speed (blue lines) and SST (red lines) at four near-shore buoy locations. The composite is made from 96 hr before to 96 hr after the start of wind events. The horizontal black line indicates 9 m s^{-1} wind speed threshold for wind events. The composite mean at each lag hr is averaged over wind events selected from April to July between 1983 and 2014. Shaded areas correspond to one standard error of the mean for wind speed/SST at each lag hr. The number of events identified at 46014(a) is 225, at 46028(b) is 265, at 46012(c) is 141, at 46013(d) is 280. The mean of wind speed between lag -96 hr and 96 hr at 46014(a) is 9.2 m s^{-1}, at 46028(b) is 9.7 m s^{-1}, at 46012(c) is 9.3 m s^{-1}, at 46013(d) is 9.9 m s^{-1}. The mean of SST between lag -96 hr and 96 hr at 46014(a) is 10.4°C, at 46028(b) is 11.6°C, at 46012(c) is 10.8°C, at 46013(d) is 10.1°C.

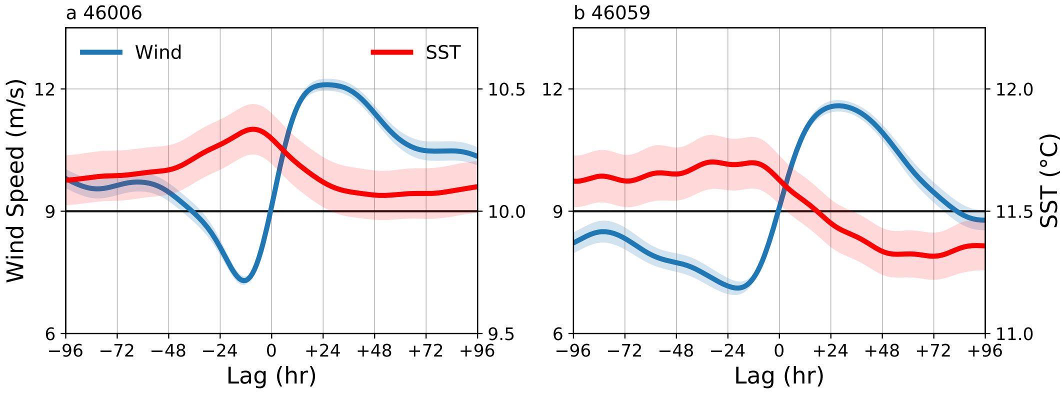

Figure 6. Evolution of composite mean of wind speed (blue lines) and SST (red lines) at two far off-shore buoy locations, where buoy 46006(a) is about 1000 km offshore and 46059(b) is about 500 km. The wind events at these two locations are selected with 9 m s^{-1} wind speed threshold without restriction on wind direction (see section 2.4 for details). The number of events identified at 46006 is 158, and at 46059 is 113. The mean of wind speed between lag -96 hr and 96 hr at 46006(a) is 10.0 m s^{-1}, and at 46059(b) is 9.1 m s^{-1}. The mean of SST between lag -96 hr and 96 hr at 46006(a) is 10.1°C, and at 46059(b) is 11.5°C.

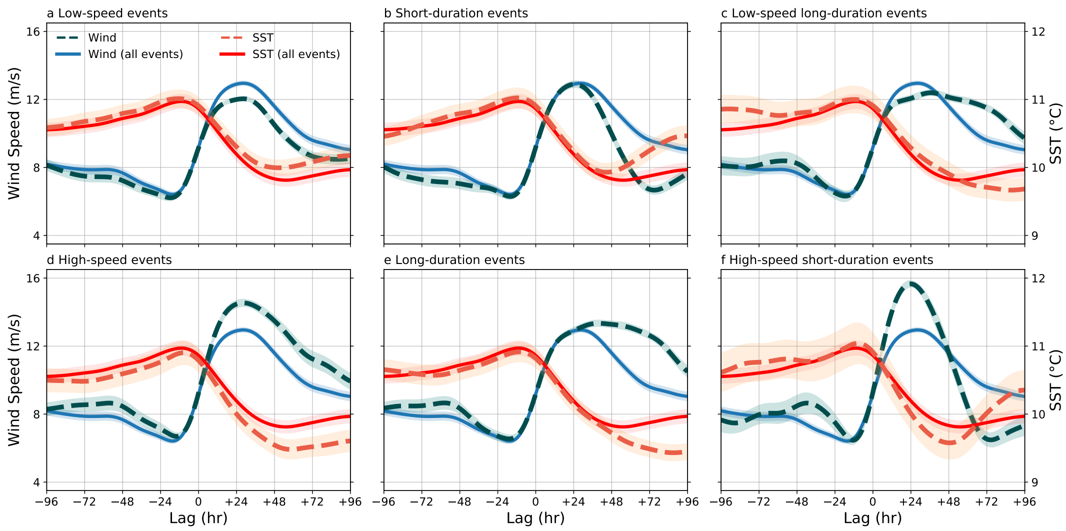

Figure 7. Evolution of composite mean of wind speed (green dashed lines) and SST (orange dashed lines) at buoy 46014 for (a) low-speed events, (b) short-duration events, (c) low-speed long-duration events, (d) high-speed events, (e) long-duration events, and (f) high-speed short-duration events. These events are identified from April to July between 1983 and 2014. Total number of events occurring at buoy 46014 is 225, and the number of events for each case is: 143(a), 115(b), 57(c), 82(d), 110(e), 29(f). The solid lines in each plot replicate the composite mean of SST (red) and wind speed (blue) over all 225 wind events at buoy 46014, shown in Figure 4a. Shaded areas correspond to one standard error of the mean for wind speed/SST at each lag hr.

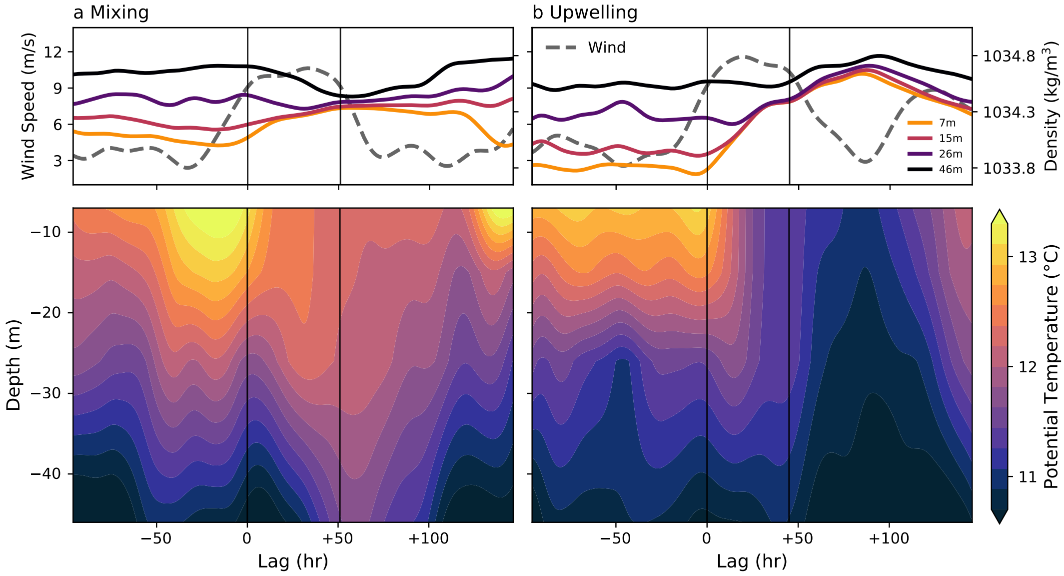

Figure 8. Time evolution of wind speed (dashed lines, upper panel), potential density at four depths (solid lines, upper panel), and potential temperature with depths (lower panel) for two wind events identified at CCE-2 mooring. (a) A wind event with a possible case of strong mixing, occurring in April 11, 2013, identified at CCE2-04. (b) A wind event with a possible case of enhanced upwelling, occurring in April 1, 2012, identified at CCE2-03. Vertical lines mark the onset and end time of the wind event.

References

Atlas, R., Hoffman, R. N., Ardizzone, J., Leidner, S. M., Jusem, J. C., Smith, D. K., & Gombos, D. (2011). A cross-calibrated, multiplatform ocean surface wind velocity product for meteorological and oceanographic applications. *Bulletin of the American Meteorological Society*, *92*(2), 157–174. `https://doi.org/10.1175/2010BAMS2946.1`

Chelton, D. B., Bratkovich, A. W., Bernstein, R. L., & Kosro, P. M. (1988). Poleward flow off central California during the spring and summer of 1981 and 1984. *Journal of Geophysical Research: Oceans*, *93*(C9), 10604–10620. `https://doi.org/10.1029/JC093iC09p10604`

Dorman, C. E., Holt, T., Rogers, D. P., & Edwards, K. (2000). Large-scale structure of the June–July 1996 marine boundary layer along California and Oregon. *Monthly Weather Review*, *128*(6), 1632–1652. `https://doi.org/10.1175/1520-0493(2000)128<1632:LSSOTJ>2.0.CO;2`

Dorman, C. E., Mejia, J. F., & Koračin, D. (2013). Impact of U.S. west coastline inhomogeneity and synoptic forcing on winds, wind stress, and wind stress curl during upwelling season. *Journal of Geophysical Research: Oceans*, *118*(9), 4036–4051. `https://doi.org/10.1002/jgrc.20282`

Edwards, K. A., Rogerson, A. M., Winant, C. D., & Rogers, D. P. (2001). Adjustment of the marine atmospheric boundary layer to a coastal cape. *Journal of the Atmospheric Sciences*, *58*(12), 1511–1528. `https://doi.org/10.1175/1520-0469(2001)058<1511:AOTMAB>2.0.CO;2`

Fewings, M. R., Washburn, L., Dorman, C. E., Gotschalk, C., & Lombardo, K. (2016). Synoptic forcing of wind relaxations at Pt. Conception, California. *Journal of Geophysical Research: Oceans*, *121*(8), 5711–5730. `https://doi.org/10.1002/2016JC011699`

Flynn, K. R., Fewings, M. R., Gotschalk, C., & Lombardo, K. (2017). Large-scale anomalies in sea-surface temperature and air-sea fluxes during wind relaxation events off the United States West Coast in summer. *Journal of Geophysical Research: Oceans*, *122*(3), 2574–2594. `https://doi.org/10.1002/2016JC012613`

Halliwell, G. R., & Allen, J. S. (1987). The large-scale coastal wind field along the west coast of North America, 1981–1982. *Journal of Geophysical Research:*

Oceans, *92*(C2), 1861–1884. https://doi.org/10.1029/JC092iC02p01861

Hsu, S. A., Meindl, E. A., & Gilhousen, D. B. (1994). Determining the power-law wind-profile exponent under near-neutral stability conditions at sea. *Journal of Applied Meteorology*, *33*(6), 757–765. https://doi.org/10.1175/1520-0450(1994)033<0757:DTPLWP>2.0.CO;2

Koračin, D., & Dorman, C. E. (2001). Marine atmospheric boundary layer divergence and clouds along California in June 1996. *Monthly Weather Review*, *129*(8), 2040–2056. https://doi.org/10.1175/1520-0493(2001)129<2040:MABLDA>2.0.CO;2

Koračin, D., Dorman, C. E., & Dever, E. P. (2004). Coastal perturbations of marine-layer winds, wind stress, and wind stress curl along California and Baja California in June 1999. *Journal of Physical Oceanography*, *34*(5), 1152–1173. https://doi.org/10.1175/1520-0485(2004)034<1152:CPOMWW>2.0.CO;2

Martz, T., Send, U., Ohman, M. D., Takeshita, Y., Bresnahan, P., Kim, H.-J., & Nam, S. H. (2014). Dynamic variability of biogeochemical ratios in the Southern California Current System. *Geophysical Research Letters*, *41*(7), 2496-2501. https://doi.org/10.1002/2014GL059332

McDougall, T. J., & Barker, P. M. (2011). *Getting started with TEOS-10 and the Gibbs Seawater (GSW) Oceanographic Toolbox.* SCOR/IAPSO WG127. http://www.teos-10.org/pubs/Getting_Started.pdf

McGillicuddy, D. J., Anderson, L. A., Bates, N. R., Bibby, T., Buesseler, K. O., Carlson, C. A., … Steinberg, D. K. (2007). Eddy/wind interactions stimulate extraordinary mid-ocean plankton blooms. *Science*, *316*(5827), 1021–1026. https://doi.org/10.1126/science.1136256

Mears, C. A., Scott, J., Wentz, F. J., Ricciardulli, L., Leidner, S. M., Hoffman, R., & Atlas, R. (2019). A near-real-time version of the Cross-Calibrated Multiplatform (CCMP) ocean surface wind velocity data set. *Journal of Geophysical Research: Oceans*, *124*(10), 6997-7010. https://doi.org/10.1029/2019JC015367

Melton, C., Washburn, L., & Gotschalk, C. (2009). Wind relaxations and poleward flow events in a coastal upwelling system on the central California coast. *Journal of Geophysical Research: Oceans*, *114*, C11016. https://doi.org/10.1029/2009JC005397

Ohman, M. D., Rudnick, D. L., Chekalyuk, A., Davis, R. E., Feely, R. A., Kahru, M., … Send, U. (2013). Autonomous ocean measurements in the California Current Ecosystem. *Oceanography*, *26*(3), 18–25. https://doi.org/10.5670/oceanog.2013.41

Roemmich, D., & Gilson, J. (2009). The 2004–2008 mean and annual cycle of temperature, salinity, and steric height in the global ocean from the Argo Program. *Progress in Oceanography*, *82*(2), 81–100. https://doi.org/10.1016/j.pocean.2009.03.004

Samelson, R. M., Skyllingstad, E. D., Chelton, D. B., Esbensen, S. K., O'Neill, L. W., & Thum, N. (2006). On the coupling of wind stress and sea surface temperature. *Journal of Climate*, *19*(8), 1557–1566. https://doi.org/10.1175/JCLI3682.1

Send, U., Beardsley, R. C., & Winant, C. D. (1987). Relaxation from upwelling in the Coastal Ocean Dynamics Experiment. *Journal of Geophysical Research: Oceans*, *92*(C2), 1683–1698. https://doi.org/10.1029/JC092iC02p01683

Small, R. J., deSzoeke, S. P., Xie, S.-P., O'Neill, L., Seo, H., Song, Q., … Minobe, S. (2008). Air–sea interaction over ocean fronts and eddies. *Dynamics of Atmospheres and Oceans*, *45*(3-4), 274–319. https://doi.org/10.1016/j.dynatmoce.2008.01.001

Taylor, S. V., Cayan, D. R., Graham, N. E., & Georgakakos, K. P. (2008). Northerly surface winds over the eastern North Pacific Ocean in spring and summer. *Journal of Geophysical Research: Atmospheres*, *113*, D02110. https://doi.org/10.1029/2006JD008053

Thomas, L. N., & Lee, C. M. (2005). Intensification of ocean fronts by down-front winds. *Journal of Physical Oceanography*, *35*(6), 1086–1102. https://doi.org/10.1175/JPO2737.1

Supporting Information for "Observed Wind and SST Variability off the California Coast During Summertime High Wind Events"

Weiguang Wu[1,2], Ana. B. Villas Bôas[1], and Sarah. T. Gille[1]

[1]Scripps Institution of Oceanography, University of California San Diego, La Jolla, CA, USA

[2]Now at MIT-WHOI Joint Program in Oceanography/Applied Ocean Sciences and Engineering, Massachusetts Institute of Technology, Cambridge, MA, USA

Contents of this file

Introduction

The first three supporting figures here show the evolution of composite mean of wind speed (green dashed lines) and SST (orange dashed lines) for different types of wind events at buoy 46013 (Figure S1), 46012 (Figure S2), and 46028 (Figure S3). The wind events are classified by: (a) Low-speed events: the 90 percentile of wind speed within the event is less than 15 m s^{-1}; (b) Short-duration events: the duration of events is less than 72 hrs; (c) Low-speed long-duration events: the duration is greater than 72 hrs and the 90 percentile speed is less than 15 m s^{-1}; (d) High-speed events: the 90 percentile speed is greater than 15 m s^{-1}; (e) Long-duration events: the duration is greater than 72 hrs;

(f) High-speed short-duration events: the duration is less than 72 hrs and the 90 percentile speed is greater than 15 m s^{-1}. These events were identified from April to July between 1983 and 2014. Events with missing data are not included in the analysis.

Figure S4 shows the vertical profiles of potential temperature anomaly (red lines) and potential density anomaly (blue lines) at top 100 dbar from an Argo climatology (Roemmich & Gilson, 2009) at nearest point to NDBC buoy 46006 (dashed lines) and buoy 46028 (solid lines). The anomalies at each depth are defined in respect to the surface values. Temperature and density anomalies at every depth are averaged between April and July from 2004 to 2018 using the Argo climatology. Note that both the stratification and temperature are similar at the two buoys locations down to pressure of about 40 dbar.

References

Roemmich, D., & Gilson, J. (2009). The 2004–2008 mean and annual cycle of temperature, salinity, and steric height in the global ocean from the Argo Program. *Progress in Oceanography*, *82*(2), 81–100. Retrieved from https://doi.org/10.1016/j.pocean.2009.03.004

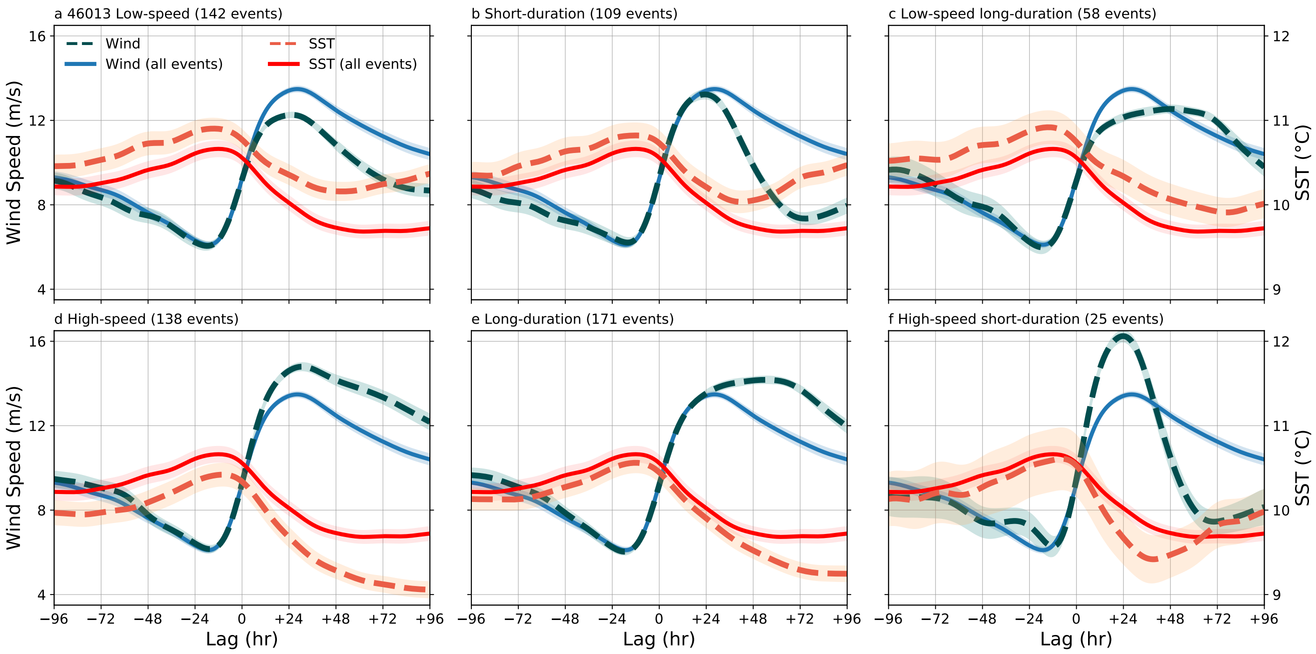

Figure S1. Evolution of composite mean of wind speed (green dashed lines) and SST (orange dashed lines) for different types of wind events at buoy 46013. The number of events for each scenario is indicated in the title. Solid lines are the same as in Fig. 5d. The red solid line in each plot is the composite mean of SST and the blue solid line is the composite mean wind speed over all wind events at buoy 46013. Shaded areas correspond to one standard error of the mean for wind speed/SST at each lag hr.

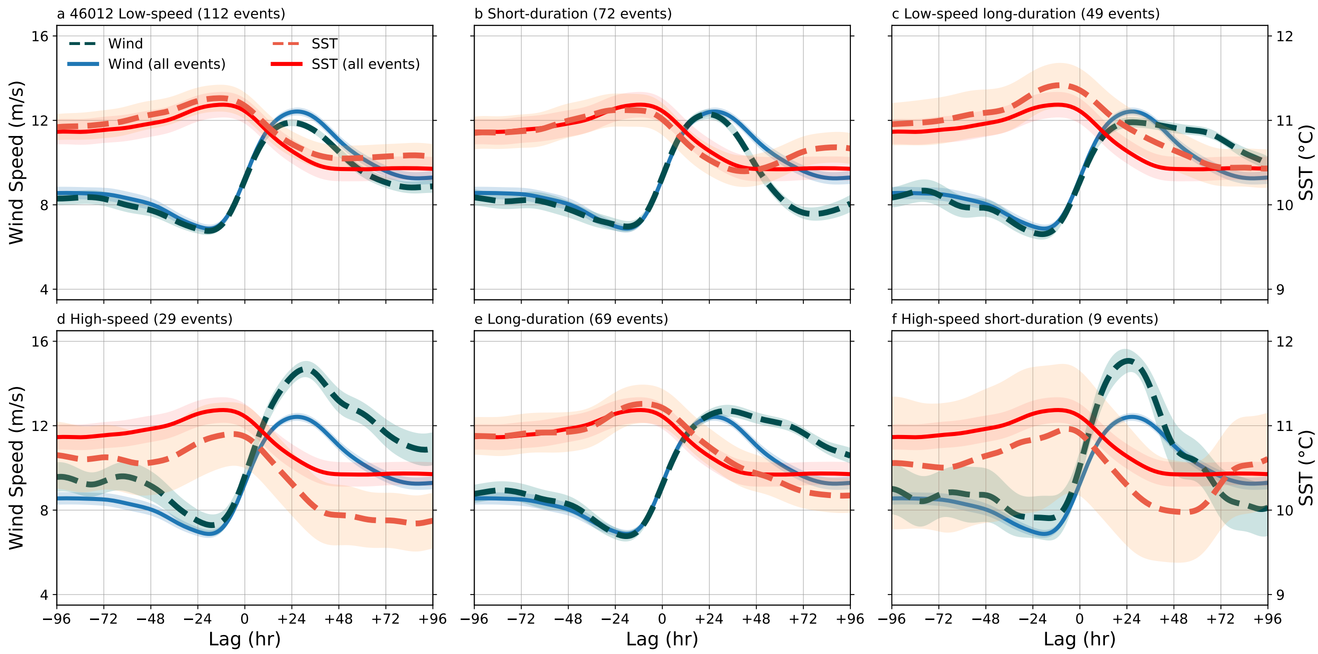

Figure S2. Evolution of composite mean of wind speed (green dashed lines) and SST (orange dashed lines) for different types of wind events at buoy 46012. The number of events for each scenario is indicated in the title. Solid lines are the same as in Fig. 5c. The red solid line in each plot is the composite mean of SST, and the blue solid line is the composite mean wind speed over all wind events at buoy 46012. Shaded areas correspond to one standard error of the mean for wind speed/SST at each lag hr.

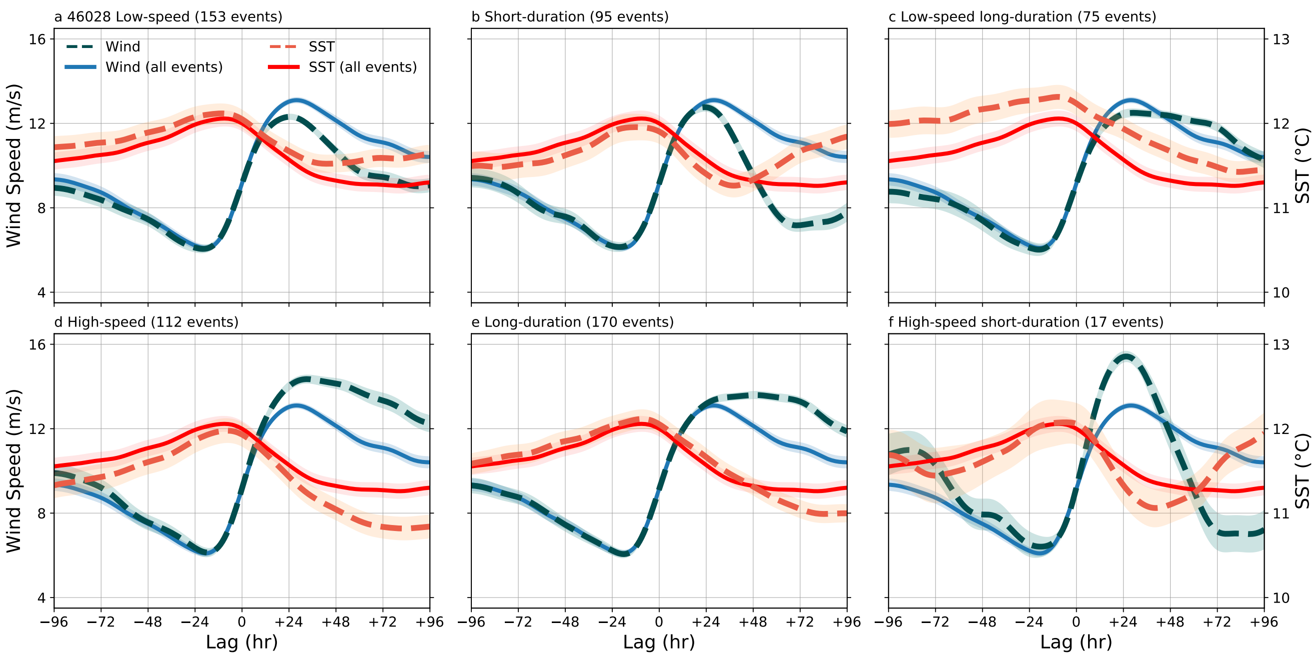

Figure S3. Evolution of composite mean of wind speed (green dashed lines) and SST (orange dashed lines) for different types of wind events at buoy 46028. The number of events for each scenario is indicated in the title. Solid lines are the same as in Fig. 5b. The red solid line in each plot is the composite mean of SST over all wind events, and the blue line is the composite mean wind speed at buoy 46028. Shaded areas correspond to one standard error of the mean for wind speed/SST at each lag hr.

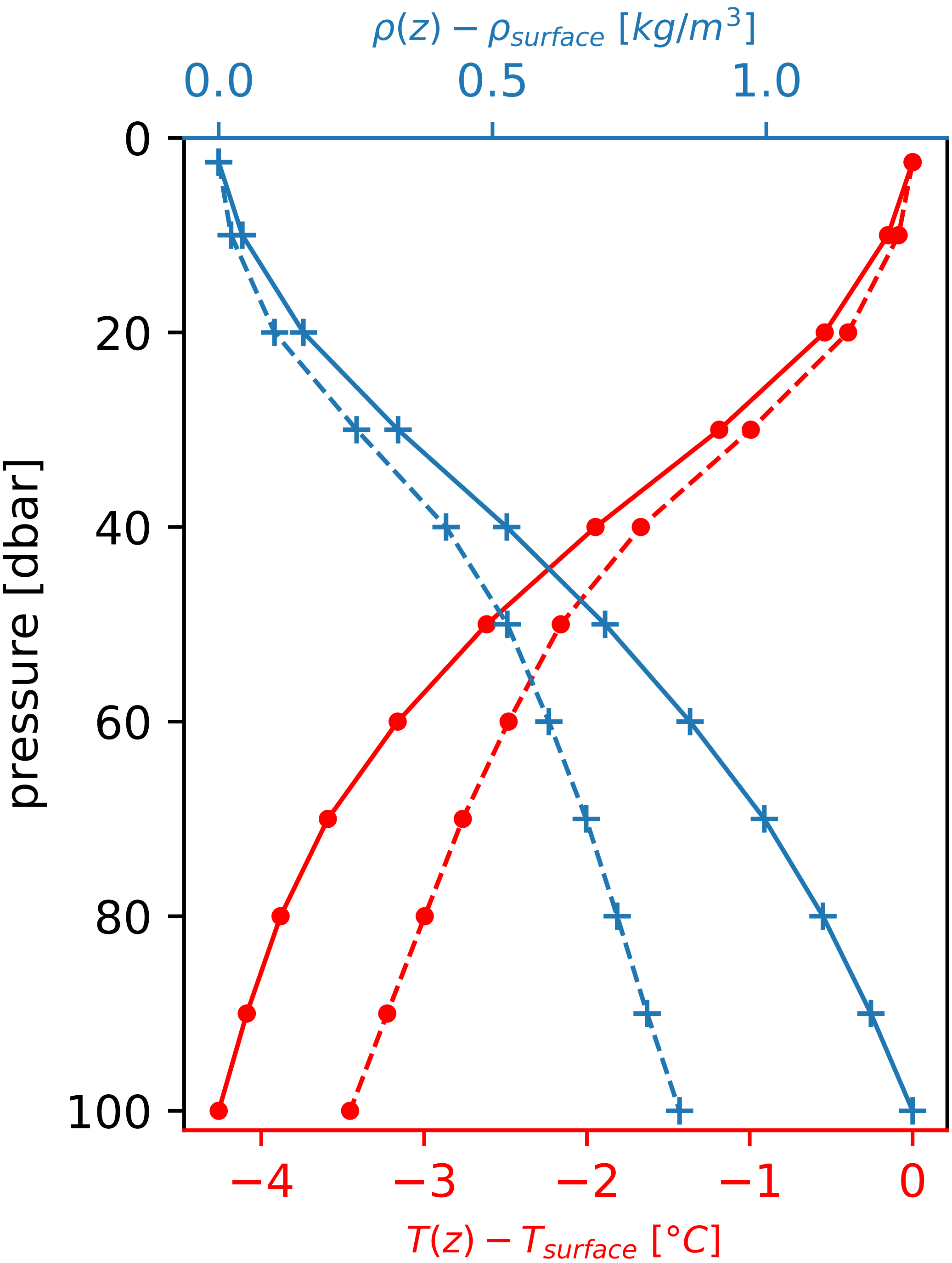

Figure S4. Vertical Argo profiles of potential temperature anomaly (red lines) and potential density anomaly (blue lines) at the nearest point to NDBC buoy 46006 (dashed lines) and buoy 46028 (solid lines). The anomalies at each depth are defined in respect to the surface values. Temperature and density anomalies at every depth are averaged between April and July from 2004 to 2018 using the Argo climatology.